Mon. Not. R. Astron. Soc. **291,** 780–796 (1997)

The effective temperature and metallicity of CM Draconis

Serena Viti,[1] Hugh R. A. Jones,[2,3] Andreas Schweitzer,[4,5] France Allard,[6] Peter H. Hauschildt,[7] Jonathan Tennyson,[1] Steven Miller[1] and Andrew J. Longmore[8]

[1]*Department of Physics and Astronomy, University College London, Gower Street, London WC1E 6BT*
[2]*Institute of Astronomy, University of Tokyo, 2-21-1 Osawa, Mitaka, Tokyo 181, Japan*
[3]*Astrophysics Group, Liverpool John Moores University, Byrom Street, Liverpool L3 3AF*
[4]*Landessternwarte Heidelberg, Königstuhl, D-69117 Heidelberg, Germany*
[5]*Department of Physics and Astronomy, Arizona State University, Box 871504 Tempe, AZ 85287-1504, USA*
[6]*Department of Physics, Wichita State University, 1845 Fairmount, Wichita, KS 67260-0032, USA*
[7]*Department of Physics and Astronomy, The University of Georgia, Athens, GA 30602-2451, USA*
[8]*Royal Observatory, Blackford Hill, Edinburgh EH9 3HJ*

Accepted 1997 July 9. Received 1997 July 4; in original form 1997 February 18

ABSTRACT

We compare observations of the binary system CM Draconis with synthetic spectra computed using the stellar atmosphere code PHOENIX. Spectroscopic observations from 0.40 to 2.41 μm, combined with photometry and the accurately known surface gravity, enable us to estimate the temperature and metallicity using detailed spectral synthesis. We find discrepancies between the analysis of the infrared and optical spectra: while the optical spectral energy distribution (SED) yields a metal-rich solution with $T_{\rm eff}=3000$ K, the infrared SED yields around 3200 K with $-0.8\leq$ [M/H] ≤ -0.6, compatible with the high space motion of the system. The low-metallicity characteristics of the infrared SED could be real, and are partly supported by a detailed analysis of the atomic lines in the optical region. Although the known incompleteness of the TiO and H_2O line lists in the models used, as well as problems with the observational data, will cause systematic errors, we suggest that CM Draconis could be a chemically peculiar system in that it cannot be modelled with solar abundances.

Key words: stars: atmospheres – binaries: spectroscopic – stars: fundamental parameters – stars: late-type – stars: Population II – infrared: stars.

1 INTRODUCTION

Low-mass stars are the most dominant objects in our Galaxy in terms of number density. They provide a probe of our understanding of main-sequence stellar evolution, and are the key in determining the boundary between stellar and substellar objects. There are few observations of known-mass, low-mass stars. Parameters such as effective temperatures, masses and metallicities, vital in determining positions in HR diagrams, remain controversial.

CM Draconis (hereafter CM Dra) is the lowest mass main-sequence eclipsing binary known (RA $=16^{\rm h}34^{\rm m}24^{\rm s}$, Dec. $=57°09'00''$, J2000, $V=12.9$ mag). It has a short period of 1.268 d (Metcalfe et al. 1996), and a large space velocity (163 km s^{-1}) and low flaring rate which suggest that it belongs to Population II (Lacy 1977). Paczyński & Sienkiewicz (1984) point out that CM Dra is an important system for cosmology, because its initial helium abundance can be determined from models of its structure. Since it is one of the faintest, smallest and least massive eclipsing main-sequence binaries so far known, its colour–luminosity relationship is a prime indicator of what happens to very low-mass stars at the bottom of the main sequence.

Some of the fundamental physical properties of the components of CM Dra have already been determined accurately. Most important are the individual masses $M_{\rm A}=0.2307\pm0.0010\,{\rm M}_\odot$ and $M_{\rm B}=0.2136\pm0.0010\,{\rm M}_\odot$, radii $R_{\rm A}=0.2516\pm0.0020\,{\rm R}_\odot$ and $R_{\rm B}=0.2347\pm0.0019\,{\rm R}_\odot$ (Metcalfe et al. 1996), and surface gravities $\log g=4.999\pm0.007$ for CM Dra A and $\log g=5.028\pm0.007$ for

CM Dra B (Jones et al. 1996). The precision of these values far exceeds those known for any other M dwarf, and this means that CM Dra should be an excellent system for comparison with model calculations; it gave us the motivation to improve the current values for the metallicity and effective temperature of the system.

Lacy (1977) found the temperature to be 3150 ± 100 K using a parallax of 0.069 ± 0.005 mas. Chabrier & Baraffe (hereafter CB95) argued that the effective temperature of CM Dra is 3300 K, based on a comparison between evolutionary models and observations. Assuming $T_{\rm eff}$ to be 3300 K, they then recalculated the parallax to be 0.063, different from the value adopted by Lacy. We note that the 'current' value for the parallax is 0.0692 ± 0.0025 arcsec (van Altena, Lee & Hoffleit 1995). CB95 also indirectly investigated the metallicity of CM Dra, finding agreement over a range of values. They found agreement between models and observations for metallicities of $-0.5 \leq [\mathrm{M/H}] \leq 0.0$ for $3086 < T_{\rm eff} < 3366$ K, where [M/H] is the ratio of metal abundance to hydrogen content in the star. However, the only published spectrum of CM Dra lends support for CM Dra to belong to Population II. Ruciński (1978) intercompared optical Mg, MgH and TiO features of CM Dra with those in six other M dwarfs; he concluded that it may be a subdwarf, but noted that the accuracy of determination is low. Finally, Gizis (1997) spectroscopically classified a series of M dwarfs and M subdwarfs, and found CM Draconis to have a solar metallicity using spectra from 0.62 to 0.74 μm.

A modern spectral measurement covering a wide spectral range is thus desirable to determine reliably the metallicity and the effective temperature. Here we make such a study (i) by comparing observed spectra from 0.40 to 2.41 μm with synthetic spectra computed for a wide range of effective temperatures and metallicities, and (ii) by comparing the photometry of the system with the photometry of other M dwarfs. We adopt a two-step direct approach:

(1) we attempt a general flux distribution fit to the models, and

(2) we attempt a detailed spectral analysis of restricted regions of the spectra.

The observations and data reduction procedures are described in Section 2. The models used are discussed in Section 3, and parameters for CM Dra are determined in Section 4. Sections 5 to 9 present the analysis and the results obtained.

2 OBSERVATIONS

Fig. 1 shows the spectrum of CM Dra from 0.40 to 2.41 μm. In the infrared spectrum (from 0.96 to 2.41 μm) the small

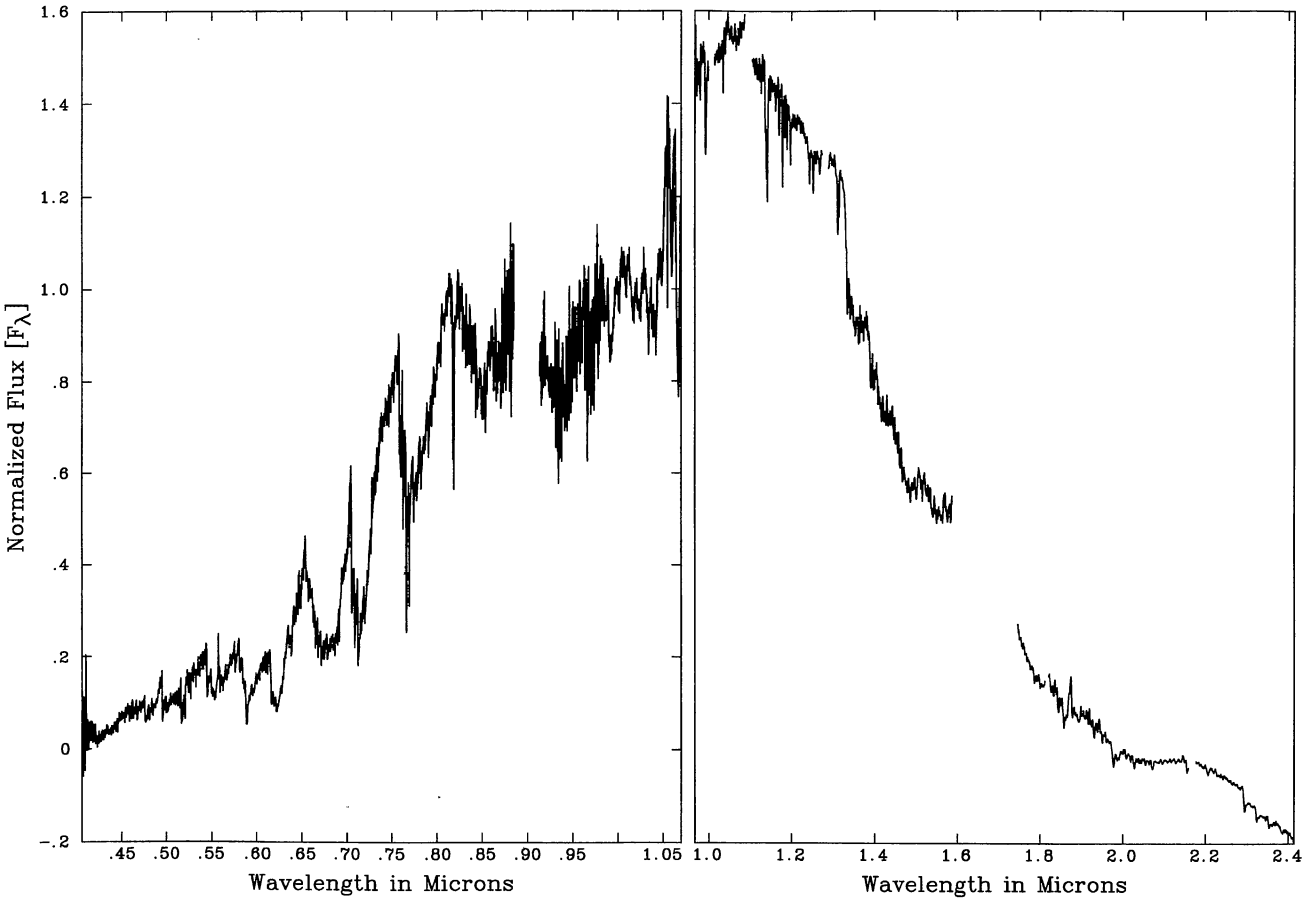

Figure 1. Spectrum of CM Draconis. Left-hand panel: optical spectrum from 0.40 to 1.07 μm. Right-hand panel: infrared spectrum from 0.97 to 2.41 μm. The region between 1.587 and 1.747 μm has not been observed. The smaller gaps are due to the hydrogen lines removed by hand.

gaps represent regions where hydrogen emission lines, introduced by the standards, were manually removed. We did not manage to observe the region centred around 1.63 μm due to a problem with the rotation of the dichroic in CGS4. We therefore adopted the differential magnitudes from Lacy (1977) to obtain the absolute flux in the *H* band. This could result in systematic errors of the absolute calibration.

2.1 Infrared observations

CM Dra was observed, along with other M dwarfs, on the nights of 1995 May 14 and 16 with the Cooled Grating Spectrometer 4 (CGS4, http://www.jach.hawaii.edu/UKIRT.new/instruments/cgs4/handbook.html) on the UK Infrared Telescope (UKIRT) on Mauna Kea, Hawaii.

CGS4 uses a 256 × 256 InSb array. Comparison sky spectra were obtained by nodding the telescope so that the object was measured successively in two rows of the array, separated by 30 arcsec. We aimed to observe throughout the three near-infrared bands *J*, *H* and *K*. The 75 line mm^{-1} grating was used with central grating wavelengths of 1.135, 1.415, 1.635 and 2.07 μm. The coverage, resolution and integration times of the observations are listed in Table 1. Each grating position overlaps with the previous and the next ones at the two ends; this ensures reliable coverage of the whole region. To remove telluric bands of water, oxygen, carbon dioxide and methane, we observed an A2p star, SAO 29931, and used it as a standard. Such stars are not expected to have any features in common with stars like CM Dra, and are mainly featureless except for some hydrogen lines. The airmass difference between the object and the standard used never exceeded 0.05, and so we are confident that the spectra have good cancellation of atmospheric features. Some of the hydrogen lines introduced into the spectrum when dividing by the standard had, however, to be removed manually. Both the object and the standard were wavelength-calibrated by using arc lines of krypton, argon and xenon. The accuracy of the calibration is around 0.5×10^{-3} μm. The sky subtraction was obtained with standard routines which eliminate any residual sky emission due to the variance of sky brightness between object and sky pairs. The signal was spread between three rows. To extract the spectrum from the sky subtracted signal an optimal extraction technique (Horne 1986) was used; this combines the rows using weights based on the spatial profile of the stellar image.

The spectra were reduced partly by using software provided for CGS4 data (Puxley, Ramsay & Beard 1992), and partly by using the FIGARO, SPECDRE and KAPPA packages provided and supported by Starlink.

Table 1. Central wavelength and wavelength coverage, resolution, dates of the observations and integration times.

λ_{cen}	λ_{range}	R	Date	Int.Time(total)
μm	μm	μm		minutes
1.135	0.96 – 1.3	0.00044	14/05/95	17
1.415	1.249 – 1.508	0.00044	14/05/95	10
1.635	1.47 – 1.8	0.00044	14/05/95	15
2.07	1.739 – 2.414	0.00088	14/05/95	10
1.415	1.249 – 1.508	0.00044	16/05/95	15
2.07	1.739 – 2.414	0.00088	16/05/95	10

2.2 Optical observations

Observations were taken during the night of 1996 July 20 at the Steward Observatory 90-inch Bok Telescope located at Kitt Peak. We used a Boller & Chivens Spectrograph with an echellette configuration consisting of 180 line mm^{-1} grating and a prism as cross-dispersor. The detector was a 1200 × 800 Loral CCD. The wavelength region covered is from 0.4 to 1.0 μm at an average resolution $\lambda/\Delta\lambda$ of 6000. The integration time of the observations was 900 s. Six orders were joined, and they were all overlapping apart from the region around 0.90 μm. To remove telluric features and instrumental fringes, the Oke standard stars (Oke 1990; Colina & Bohlin 1994) SAO 29931 (A2p), BD + 33°2642 (B2) and BD + 25°4655 (O) have been used. BD + 33°2642 and 25°4655 were also used to flux-calibrate the spectrum, although the absolute flux calibration is not reliable since the night was not photometric due to the presence of cirrus clouds. To obtain an absolute calibration, the single orders have been calibrated using Lacy's photometry (1977). Both the object and the standards were wavelength-calibrated by using arc lines of HeAr. The wavelength calibration is accurate to $\sim 0.01 \times 10^{-3}$ μm. The data reduction was performed using the IRAF package.

We cannot entirely rely on the reddest part of the optical spectrum for the following reasons.

(1) Many telluric features are difficult to remove and cause substantial noise. Some contaminate important atomic lines such as the Na I 0.819-μm line and the potassium K I 0.768-μm doublet.

(2) From 0.84 to 1.0 μm we did not manage to correct completely for strong instrumental fringes.

2.3 Phase information

Our spectroscopic measurements of CM Dra were made at a variety of different phases, causing the spectra on which this analysis is based to be composite with different spectral regions having different relative contributions from the A and B components. We calculated the phase at which the system was during the observations.

For the UKIRT observations on the first night (1995 May 14) we observed the regions centred at 1.135, 1.415 1.635 μm when one component was fully visible together with ~ 85 per cent of the other. During the integration time of the obsevation of the region centred at 2.07 μm one component was fully visible together with ~ 80 per cent of the other. On the second night of observations (1995 May 16) we observed the regions centred at 1.415 and 2.07 μm when one component was fully visible together with ~ 60 per cent of the other. The optical region was also observed during the latter phase.

We note that when integrating the flux density, as described below, and when performing the spectral analysis we have not taken account of the phase at which spectral observations of CM Dra were made. We choose not to use this information because (1) we do not feel confident that the accuracy of our spectral photometry is better than 30 per

cent, and (2) the components will be very similar; for example, the measurements of Lacy (1977), on which much of this analysis depends, could not distinguish a difference in the temperature between A and B.

3 MODELS

Model spectra were computed for this project with the model atmosphere code PHOENIX using direct opacity sampling treatment of the opacity of H_2O as described in Allard et al. (1994). H_2O and TiO are the primary opacity sources governing the energy output of cool stars. Their importance has led to a number of groups finding the opacities for these molecules in conditions appropriate to cool stars. The data used here include the Miller–Tennyson (Miller et al. 1994; Schryber, Miller & Tennyson 1995) water vapour line list. The model of Allard et al. (1994) was augmented by using the improved Collins–Jørgensen TiO line list (Collins & Faij 1974; Jørgensen 1994). Since the surface gravity of the CM Draconis pair is close to $\log g = 5.0$, we have investigated model spectra in the effective temperature and metallicity parameter spaces for this value of gravity only.

After completion of this work, the more recent NextGen model structures became available. We have therefore undertaken some tests with these latest models. Although we noticed improvements in the optical fit, which is most sensitive to changes in the model structure, we find nothing that would alter the conclusions of this paper. An extensive review of the models and their properties can be found in Allard et al. (1997).

In this work we use model temperatures from 3000 to 3400 K and metallicities from $[M/H] = -1.0$ to $+0.2$. For $T_{\rm eff} = 3150$ K, two models at $[M/H] = -1.5$ and -2.0 were also computed. The parameters represent the probable extremes of metallicity and effective temperature of CM Dra. The rotational velocity has also been calculated, with the latest values for the period and radii yielding a value of $v_{\rm rot} = 10 \pm 0.02$ km s^{-1}, in agreement with Metcalfe et al. (1996). This means that any change induced by rotation in the models would be negligible at the resolution of our observations, as even our highest resolution observations only have a resolution of 50 km s^{-1}.

We have not tried comparing the system with models computed with non-solar abundance patterns.

Jones et al. (1996) investigated the sensitivity of observations of M dwarfs and a previous generation of these models to changes in effective temperature and gravity over a small region from 1.16 to 1.22 μm. With data of similar resolution, we first investigate the sensitivity of the synthetic spectra to changes in temperature and metallicity for the region from 1.0 to 2.4 μm, noting that, unlike the study of Jones et al. (1996), the precision to which the gravity is known for CM Dra means that we can ignore it as a variable in the analysis. Figs 2(a)–(d) show samples of such an investigation. In (a) and (b), two models have been normalized to have the same mean value and plotted together; in (c) and (d) the two models have been divided by one another. The models were selected in such a way as to show the two extremes in each parameter. From Figs 2(a) and (b) it can be seen that a change in temperature affects the water absorption (see, for example, the regions centred at 1.4 and 1.9 μm). Water dissociates at high temperatures, and the absorption bands are weaker. Figs 2(c) and (d) show some sensitivity to a change in metallicity; however, the weaker absorption lines, which are not affected as much by blending effects, seem to be sensitive enough to variations in the metallicity for us to discriminate between models. Significant metallicity sensitivity can be seen in the prominent 2.21-μm Na I and 2.29-μm CO band features.

4 CM DRA PARAMETERS

We adopt the recently derived values for the radii of CM Dra from Metcalfe et al. (1996) to calculate an effective temperature for the system. To derive the total luminosity we adopt a parallax of 0.0692 ± 0.0025 arcsec (van Altena, Lee & Hoffleit 1995). We obtain the total absolute flux of the system by integrating the flux density over the total spectral region from 0.1 to 100 μm obtained by normalizing the infrared and optical observed spectra to Lacy's photometry for the ultraviolet and far-infrared bands and by using a synthetic spectrum to add the missing parts of the spectrum (we used a $T_{\rm eff} = 3300$ K, $[M/H] = -0.8$ model). In particular, we do not consider the flux calibration of the optical and infrared spectra sufficient to warrant adjustments of each spectrum to allow for the orbital phase (discussed above). Fig. 3 shows the overall observed spectral energy distribution (SED) of CM Dra.

We thus derive a total luminosity of $(9.36 \pm 0.67) \times 10^{-3}\,L_\odot$ [$L_A = (4.998 \pm 0.504) \times 10^{-3}\,L_\odot$ and $L_B = (4.362 \pm 0.441) \times 10^{-3}\,L_\odot$]. This implies effective temperatures for CM Dra A and CM Dra B of 3073 ± 57 and 3076 ± 57 K respectively. The derived effective temperatures are not consistent with the effective temperature of the model employed for making up the missing parts of the spectrum. However, the amount of flux deduced by the model is negligible with respect to the flux derived from the optical and infrared spectra. Considering the calibration problems in adding different pieces of information to make up a complete spectrum for CM Dra, we believe that 250-K inconsistency is acceptable. Lacy calculated the effective temperature to be 3150 ± 100 K: by employing the more accurate values for the radii by Metcalfe et al. we reduced the error by 40 per cent. With the new values of the radii and period from Metcalfe et al. (1996) we also calculated the orbital velocities of the two components. See Table 2 for a summary of CM Dra parameters.

5 PHOTOMETRIC ANALYSIS

The CM Dra system appears to be a normal member of the solar-metallicity main sequence in the M_V versus $V-I$ colour–magnitude diagram. This is portrayed in Fig. 4(a), where the photometry of the unresolved system by Leggett (1992) has been corrected to reflect the photometry of each component, and is compared to a sample of M dwarfs and metal-poor field stars by Monet et al. (1992). Most M dwarfs fit along a well-defined sequence, reproduced here by an arbitrary straight line to accentuate its location. Some objects, like CM Dra itself, appear overluminous with respect to this sequence due to added brightness from an unresolved companion. If we assume that both companions of the CM Dra system are equally bright, the resulting

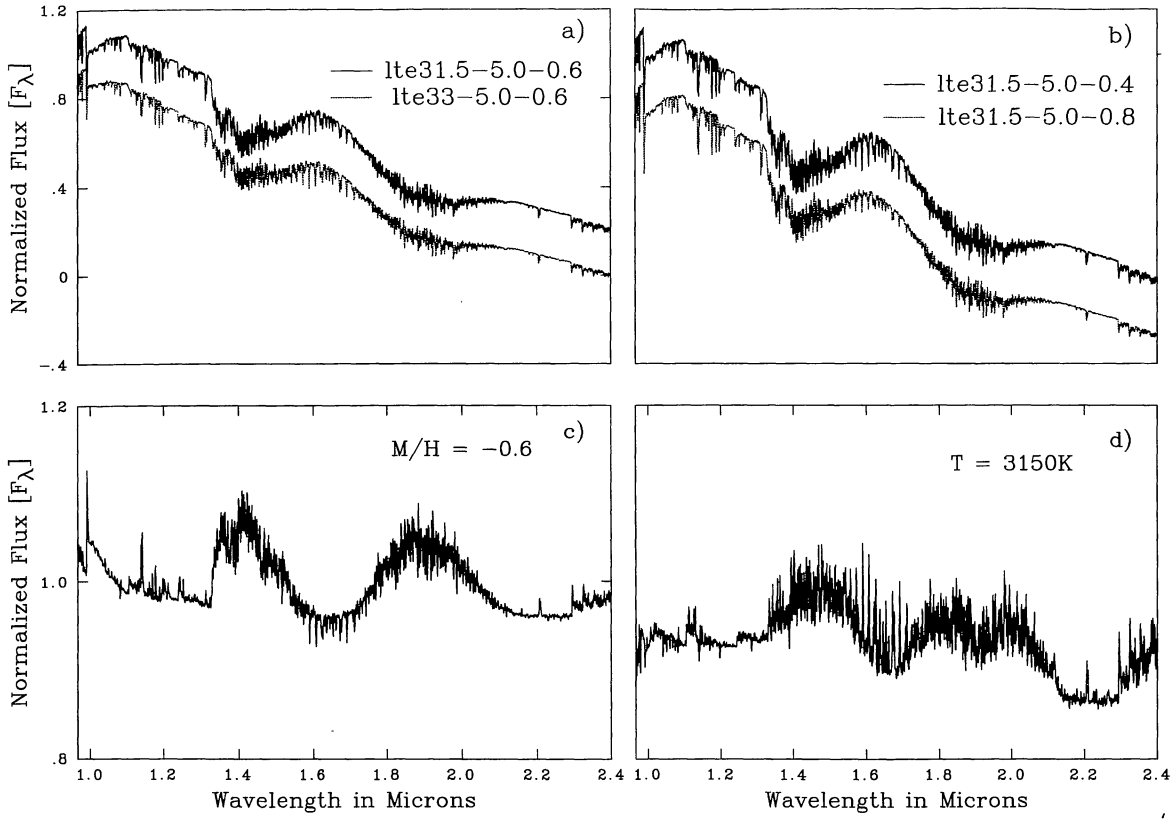

Figure 2. Sensitivity of the models to changes in $T_{\rm eff}$ and [M/H]. The different models are distinguished using the notation lteTT-G.G-Z.Z, where lte = local thermodynamic equilibrium assuming ζ(LTE) = 2 km s^{-1}, TT = $T_{\rm eff}$/100 K, G.G = log$g$ (surface gravity), Z.Z = [M/H] (metallicity), where [M] $\equiv \log M_{\rm star} - \log \mathrm{M}_{\odot}$ for any abundance quantity M. Top left: comparison of the $T_{\rm eff}$ = 3150 K model with the $T_{\rm eff}$ = 3300 K one at a fixed metallicity, [M/H] = −0.6. The y axis of the 3300-K model has been shifted by 0.2 for clarity. Bottom left: the 3150-K model divided by the 3300-K one. Top and bottom right: same as left but comparing [M/H] = −0.4 with [M/H] = −0.8 for a fixed $T_{\rm eff}$ = 3150 K.

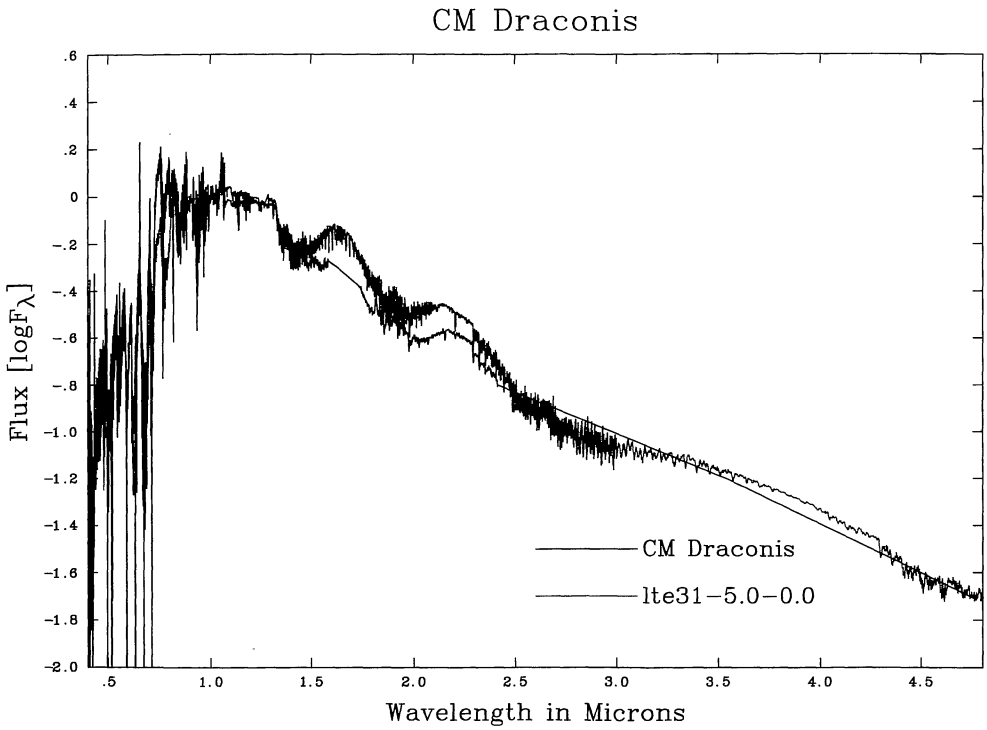

Figure 3. The overall spectral energy distribution for CM Draconis from 0.4 to 5.0 μm, obtained by joining the observed optical and infrared spectra, is compared with a solar-metallicity model at $T_{\rm eff}$ = 3100 K.

Table 2. Luminosities, effective temperatures, rotational velocity and orbital velocities of CM Dra A and B.

	L ($L_\odot$)		T_{eff} (K)		v_{rot} (km)	V_{orb} (km)
	This work	Lacy (1977)	This work	Lacy (1977)		
A	$(4.9981 \pm 0.504) \times 10^{-3}$	$(5.5 \pm 0.8) \times 10^{-3}$	3073 ± 57	3150 ± 100	10	5.7124
B	$(4.3619 \pm 0.441) \times 10^{-3}$	$(4.8 \pm 0.7) \times 10^{-3}$	3076 ± 57	3150 ± 100		5.3287

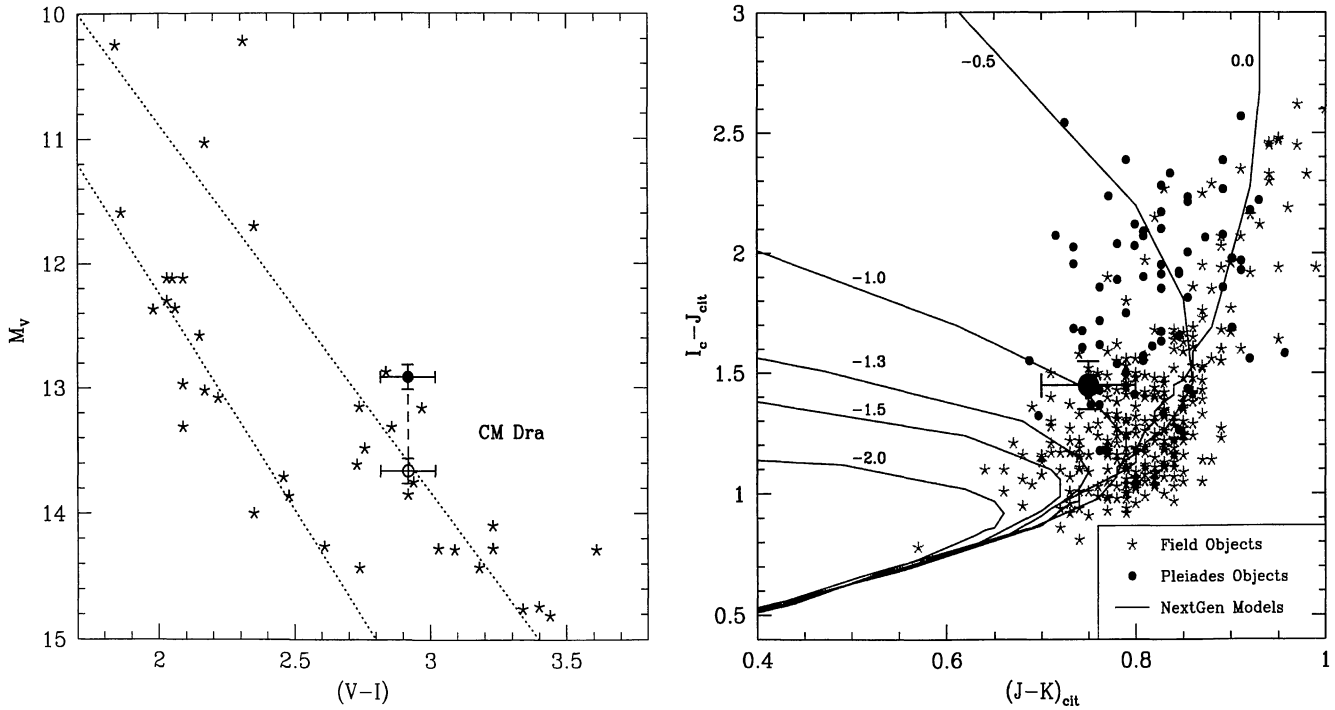

Figure 4. Left-hand panel: comparison of CM Dra according to Leggett (1992) with a sample of field M dwarf and subdwarf stars from Monet et al. (1992). We have assumed photometric errors of 0.1 mag in each filter. Unresolved binarity causes the twin pair CM Dra to lie 0.75 mag brighter than each individual component. Arbitrary loci (dotted lines) are drawn to accentuate the location of the main sequence for both the solar-metallicity (lower) and subluminous metal-poor (upper) stellar samples. Right-hand plot: the CM Dra system according to Leggett (1992) is compared to the sample of field stars from Leggett (1992), and a sample of young stellar members of the Pleiades cluster (Steele, Jameson & Hambly 1993). Unresolved binarity may translate in this diagram to a red excess in $J-K$. The 10-Gyr NextGen model isochrones (see Baraffe et al. 1997) are also shown for comparison, ranging in metallicity from [M/H] = 0.0 to −2.0, and T_{eff} = 7000 K (lower-left corner) to 2000 K.

0.75-mag shift brings the components into close agreement with the solar-metallicity main-sequence locus. Errors in the parallax or photometry well beyond those quoted above would be required to bring the high proper motion binary to resemble low-metallicity subdwarfs in this colour–magnitude diagram. The low-metallicity nature of the CM Dra binary is clearly apparent when compared to other field stars in infrared colour–colour diagrams. Fig. 4(b) compares the unresolved binary to a similar sample of field dwarfs from Leggett (1992) in the $I-J$ versus $J-K$ diagram. Leggett et al. (1996) have shown that metal-poor, high proper motion stars tend to lie above the main sequence in this diagram. Indeed, the NextGen models now suggest that the $I-J$ colour is an excellent metallicity indicator: metal-poor sequences curl back to blue $J-K$ colours as T_{eff} decreases, due to the growing pressure-induced H_2 opacities depressing the flux in the K bandpass. CM Dra lies 0.4 mag above the solar-metallicity model sequence which reproduces comfortably the bulk of the metal-rich field stars. The infrared colours of the system are more similar to those of young stars of the Pleiades cluster which appear systematically bluer than the Galactic disc main sequence. Yet both the proper motion and the gravities derived dynamically argue against a young age for CM Dra. Rather, CM Dra shows all the characteristics of metal-poor subdwarfs and coincides with 10-Gyr models of [M/H] = −1.0!

This inconsistency between the optical and infrared behaviour appear *intrinsic* to the CM Dra stellar components and suggests that the systems may have non-solar abundances ratios. Another less likely possibility is that large errors have occurred in the measurement of the parallax or optical photometry of the system. A more detailed spectroscopic analysis is required to confirm this situation.

6 OPTICAL SPECTRAL ANALYSIS

Since the observations were at slightly lower resolution than the models, we matched the latter to the instrumental resolution by smoothing with a triangular function and resam-

pling. This mimics the effect of detection by the square pixels used by the detector and three times oversampling employed for the observations. The smoothing was performed using routines within the KAPPA and SPECDRE packages. We attempt an analysis divided in two sections: the general flux distribution comparison and a more detailed spectral analysis.

6.1 General flux distribution analysis

We tried to find the best match in metallicity for each effective temperature and vice versa. We found that the best model fit is reached at a low temperature, as low as 3000 K. For low-temperatures models, some absorption bands are better fitted by low-metallicity models. For example, the synthetic flux around ~ 0.72 μm (which is due to a band of TiO) is too high in models at solar metallicities. High-temperature models give a worse fit for low metallicities: for example, for $T_{\rm eff} \geq 3150$ K, the Na I line absorption feature at 0.58 μm is better matched by the solar metallicity model. Fig. 5 shows examples at 3100 and 3300 K for low and high metallicities. Table 3 shows the best matches reached by keeping one parameter fixed. These comparisons were made twice: (1) using only the normalized optical spectrum, and (2) using the normalized infrared and optical spectra together.

6.2 Detailed spectral analysis

Due to the presence of many telluric features, the 0.87–0.91 μm region was excluded. The sample of lines were chosen from the line identification provided by PHOENIX. In the region 0.41–0.87 μm we found two very metallicity-sensitive doublets: the K I 0.768-μm doublet and the Na I

Table 3. Upper: best metallicity match within each effective temperature from a SED comparison with the optical observed region. Lower: best effective temperature match within each metallicity from a SED comparison with the optical observed region.

$T_{\rm eff}$	3000	3100	3150	3200	3300	3400
0.0						⋆
−0.2				⋆		
−0.4			⋆		⋆	
−0.6		⋆				
−0.8	⋆					
−1.0	⋆					

$[M/H]$	+0.2	0.0	−0.2	−0.4	−0.6	−0.8	−1.0
3000							
3100							⋆
3150				⋆	⋆	⋆	⋆
3200	⋆	⋆	⋆	⋆		⋆	
3300		⋆	⋆				
3400							

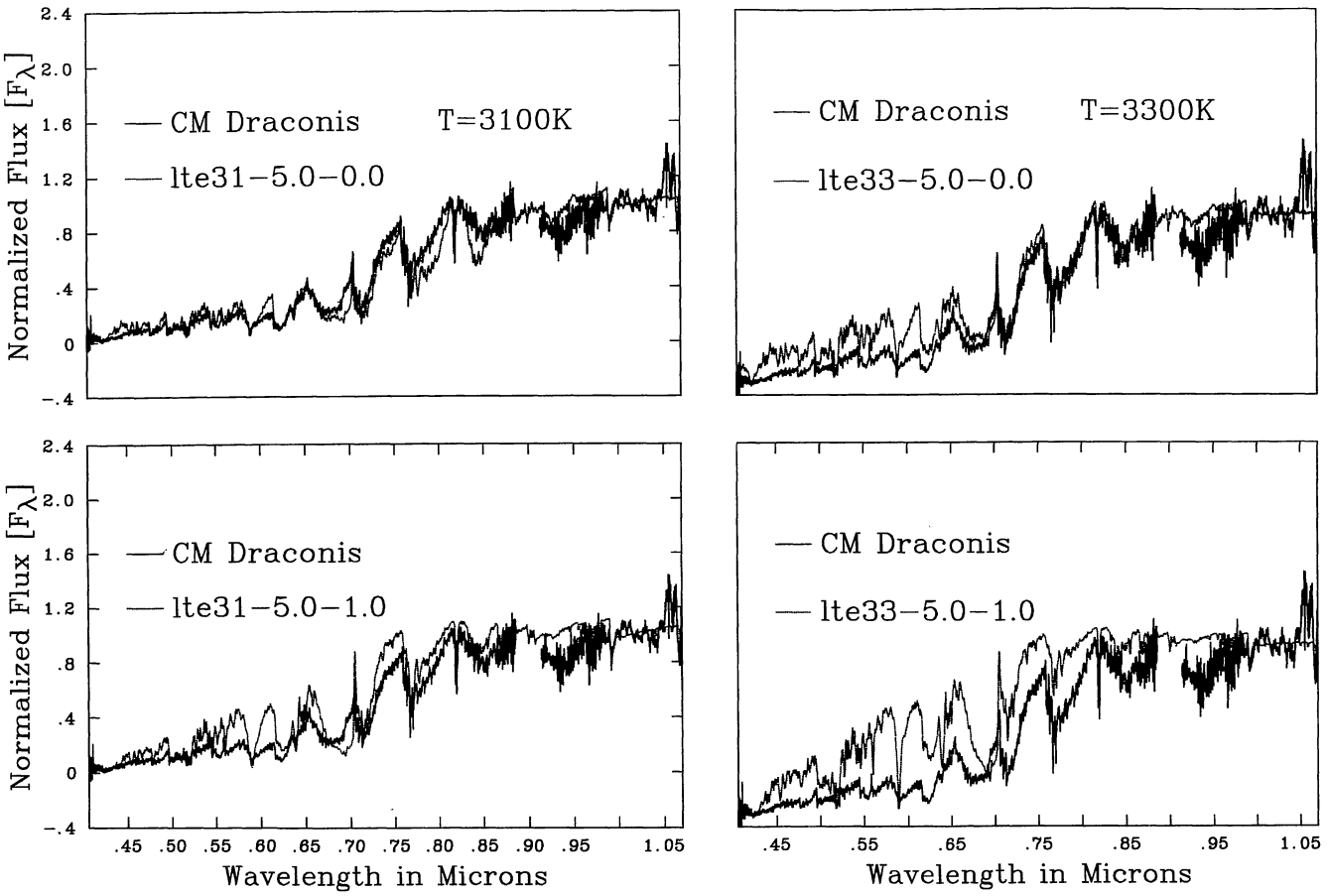

Figure 5. SED comparisons between observed spectra and models at $T_{\rm eff}$=3100 and 3300 K for [M/H]= −0.0 and −1.0 for the optical region.

0.819-μm doublet. Fig. 6 gives an example of two metallicities within the same temperature of 3000 K. Within each temperature we found the best metallicity match (see Table 4).

In general, the best metallicity lies between −0.6 and −0.8. However, with increasing temperature the fits to low-metallicity models (≤ -0.4) get worse. Note, however, that chromospheric activity could fill in the core of the resonance lines and result in apparently weaker spectral lines, resulting in a lower derived metal abundance. In addition, uncertainties in the level of the pseudo-continuum will also add systematic errors. This can be resolved with higher resolution observations that allow one to simultaneously fit the atomic and some of the molecular lines.

Choosing the best metallicity within each temperature, we compared the different temperatures and found that ~3200-K models give the best match. Fig. 7 shows an example of 3100- and 3200-K models at their 'best' metallicity, i.e., [M/H] = −0.6. Above 0.92 μm, we found a sensitive FeH absorption band centred at ~0.99 μm: this band appears sufficiently independent of the continuum for us to try a profile fit. The results of this fit are as follows.

(1) For every temperature, apart from $T_{\rm eff}$ = 3300 K, the best fit is obtained at solar metallicities. The rest of the metallicities give too strong an FeH band.

(2) Increasing the temperature causes the difference arising from a change in metallicity to decrease.

(3) At $T_{\rm eff}$ = 3300 K, the solar-metallicity model underrepresents the FeH band, while the −0.6/−0.8 models give the best fit. However, at this temperature the sensitivity of the FeH band to changes in metallicity is very small. Fig. 8 shows the fit to the FeH band for $T_{\rm eff}$ = 3100 K at [M/H] = 0.0 and −1.0, and for $T_{\rm eff}$ = 3300 K at [M/H] = 0.0 and −0.8. We note that an FeH line list is presently not available, so that the models have to use the JOLA (Just Overlapping Line Approximation; Allard & Hauschildt 1995) with astrophysical *f*-values, which are not very accurate, and therefore the modelled FeH bands cannot presently be used as reliable indicators.

In summary, from the analysis of the optical spectrum we find that low-temperature models ($T_{\rm eff}$ ~ 3000 K) of solar metallicity give a generally better SED fit. This is in agreement with the effective temperature derived previously from the luminosity and radii, and in agreement with published optical colours of CM Dra which place the system on the red edge of the disc main sequence. The detailed spectral analysis of the atomic lines in the optical spectrum leads to a slightly higher effective temperature, $T_{\rm eff}$ = ~3200 K, and a metallicity of ~ −0.6 seems to be generally the best match for many atomic lines.

7 INFRARED SPECTRAL ANALYSIS

The synthetic spectra were computed at much higher resolution than the observations, so we matched them to the

Table 4. Best metallicity match within each effective temperature after a detailed spectral analysis of the optical observed region.

$T_{\rm eff}$	3000	3100	3150	3200	3300	3400
0.0						
−0.2						
−0.4					⋆	⋆
−0.6	⋆	⋆	⋆	⋆		
−0.8				⋆		
−1.0						

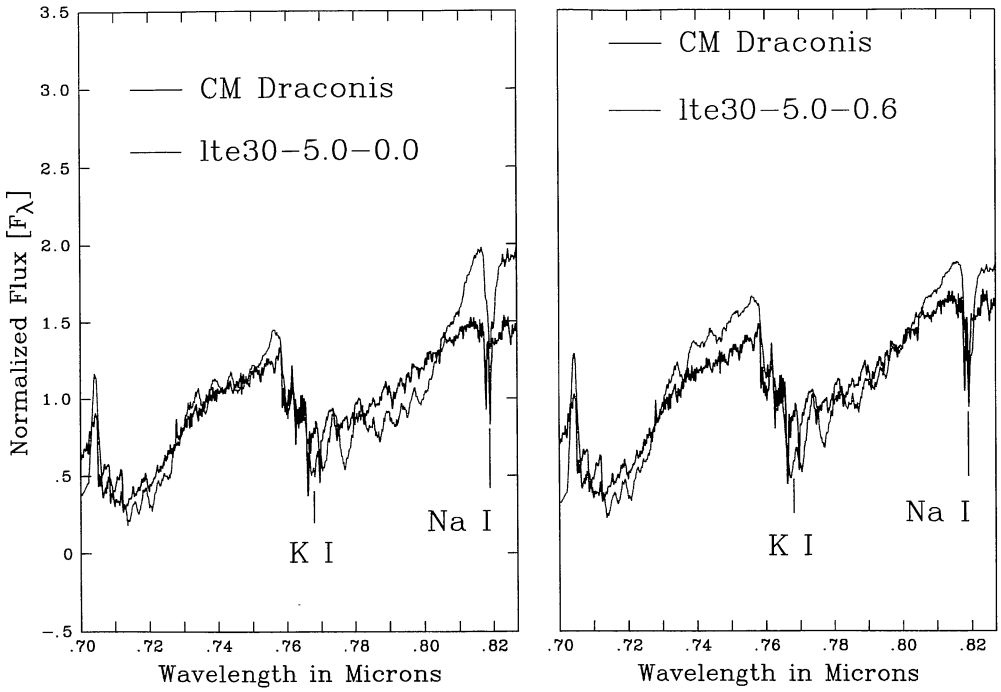

Figure 6. Sensitivity to changes in metallicities in the 0.70–0.83 μm region. Left-hand panel: $T_{\rm eff}$ = 3000 K, [M/H] = 0.0. Right-hand panel: $T_{\rm eff}$ = 3000 K, [M/H] = −0.6.

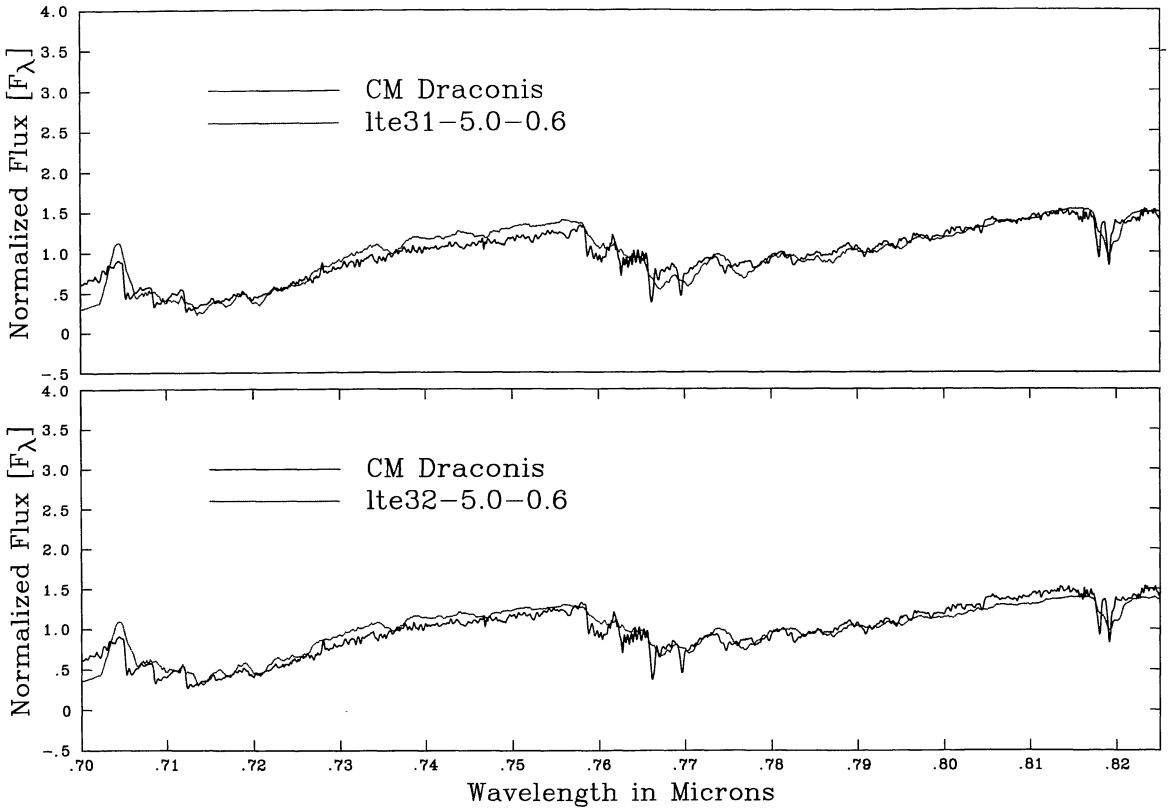

Figure 7. Comparison of observed spectrum with two models at $T_{\rm eff}=3100$ K (top plot) and $T_{\rm eff}=3200$ K (bottom plot) for a metallicity of [M/H] $=-0.6$.

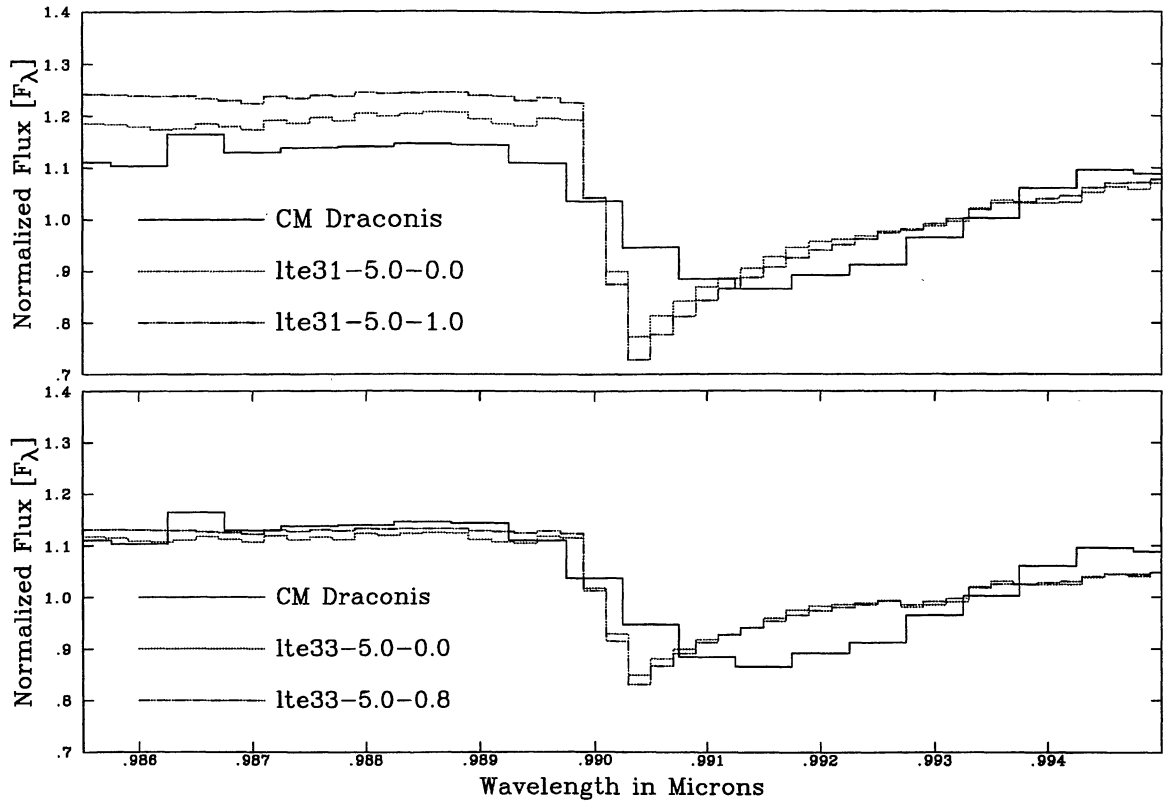

Figure 8. Fit to the FeH band centred at ~ 0.992 μm for the $T_{\rm eff}=3100$ K, [M/H] $=0.0, -1.0$ models (top plot) and for the $T_{\rm eff}=3300$ K, [M/H] $=0.0, -0.8$ models (bottom plot).

instrumental resolution by smoothing with a triangular kernel. The smoothing was performed in the same way as for the optical comparisons. Although the coverage, resolution and signal-to-noise ratios of the observations are unprecedented for M-dwarf observations, it is still not high enough to detect many of the weak absorption features which are very important in determining the best model fit. In addition, the water line list that we have used in the models is incomplete, and therefore cannot completely reproduce the infrared pseudo-continuum. This will result in systematic differences between the optical and infrared analyses. We performed our analysis in three parts.

(1) Comparison of the general flux distribution of all the models with observations. This reduced the range of possible metallicities.

(2) Analysis of the strong, clearly visible metal lines identified by Leggett et al. (1996). This step reduced the range of possible temperatures.

(3) Finally, we identified several weak lines found in the synthetic spectra. By careful analysis of their match with the observed lines we found the best match for effective temperature and metallicity.

7.1 General flux distribution comparison

The infrared spectral distribution of CM Dra is much steeper than that of typical disc M dwarfs with a $J-K$ colour nearly 0.2 mag bluer, at the same $I-J$ colour, than the bulk of the M-dwarf sample of Leggett (1992). Figs 9(a)–(d) show comparisons between models and observations at low and high metallicity for two temperatures. (a) and (b) show the comparison at $T_{\rm eff}=3100$ K for [M/H] $=-0.2$ and [M/H] $=-1.0$. (c) and (d) show the same comparison for $T_{\rm eff}=3300$ K respectively.

For a given temperature, low metallicities reproduce the infrared flux distribution better than the high ones. In fact, we found that for all temperatures the best metallicity ranges seem to be for [M/H] ≤ -0.4. However, at very low metallicities ([M/H] ≤ -1.5) the flux distribution match worsens. Fig. 10 shows a model computed at $T_{\rm eff}=3150$ K and [M/H] $=-2.0$. The water bands longward of 1.60 μm are too weak, and the CO bands in the region from 2.29 to 2.40 μm are not well reproduced. Table 5 shows the best metallicity for each effective temperature and the best effective temperature for each metallicity.

Since the present models use an incomplete water line list (Allard et al. 1994; Jones et al. 1995) which affects the quality of the fits, we have performed the fits by eye, avoiding spectral regions which we know are not reproduced adequately by the models. Although the general flux distribution of the observed spectrum is reasonably well matched by the models, we do not believe that the line-by-line comparison is sufficiently accurate for a χ^2 fit to be useful. In addition, calibration problems will introduce systematic errors that will increase the uncertainty of the derived parameters.

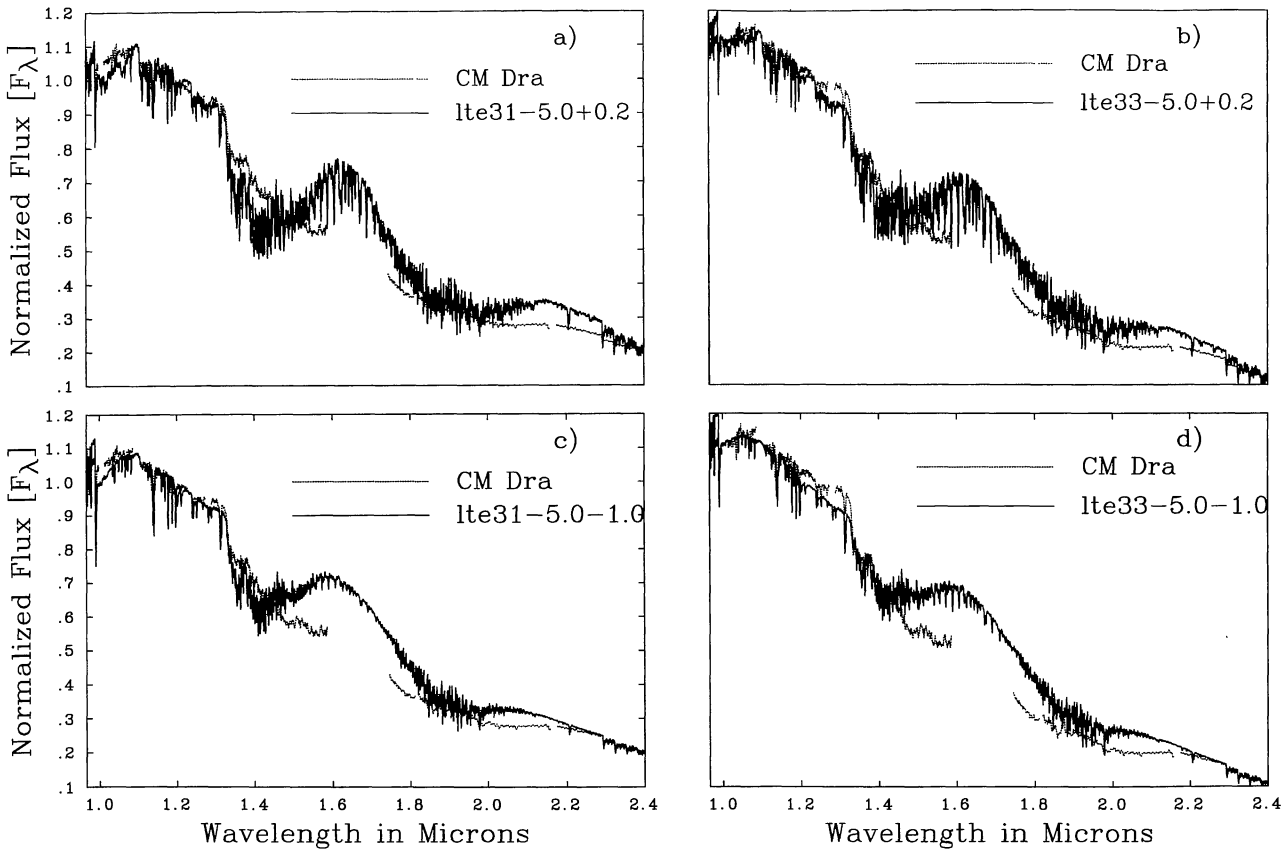

Figure 9. Spectral energy distribution (SED) comparisons between synthetic and observed spectra at $T_{\rm eff}=3100$ K, [M/H] $=+0.2$ (top left); $T_{\rm eff}=3100$ K, [M/H] $=-1.0$ (bottom left); $T_{\rm eff}=3300$ K, [M/H] $=+0.2$ (top right); $T_{\rm eff}=3300$ K, [M/H] $=-1.0$ (bottom right). The units of the normalized flux are in erg s^{-1} cm^{-2} Å^{-1}.

The above analysis does not absolutely rule out any of the trial effective temperatures, although 3000- and 3100-K models give a worse match. Our results appear to be in agreement with CB95 in that the $T_{\rm eff}=3300$ K models match the observations better. However, this agreement is somewhat misleading, since CB95 used the 'Base' grid of model atmospheres of Allard & Hauschildt (1995) which caused the interior models to yield a cooler effective temperature at a given mass than the more recent NextGen models.

In contrast to CB95, we do not find at lower temperatures that the high-metallicity models agree better with the observations. Indeed, although there is a better match at low metallicity for models of all temperatures, the 3300-K models show the least sensitivity to changes in metallicities. It is therefore more difficult to exclude high metallicities at higher temperatures with the current data.

As a consequence of the water opacity problem, no real choice of parameters could be made based only on the match of the general flux distribution. The shape of this distribution is likely to be strongly dependent on the shape of hot vibrational water bands (see Jones et al. 1995), a problem which might soon be resolved by new water line lists that are currently being tested. However, the observed infrared SED indicates a subsolar mixture for the system.

7.2 Strong lines – identification and analysis

We divide our spectral region in four subregions:

0.97–1.16 μm,

1.16–1.2 μm,

1.2–1.35 μm, and

2.2–2.4 μm.

The region between 1.35 and 2.20 μm is excluded, since it is dominated by the water bands and therefore not reliable for detailed comparison. We used Leggett et al.'s (1996) list of strong atomic lines for our analysis.

Fig. 11 confirms the result of the previous section at both $T_{\rm eff}=3150$ and 3300 K, in the region from 2.2 to 2.5 μm. In particular, the CO bands at ~ 2.353 μm are well matched by the model at $T_{\rm eff}=3300$ K, [M/H] $=-1.0$. In fact, the CO bands at 2.29 and 2.32 μm are far too strong in all models,

Table 5. Upper: best metallicity match within each effective temperature as seen from a SED comparison with the infrared observed region. Lower: best effective temperature match within each metallicity as seen from a SED comparison with the infrared observed region.

$T_{\rm eff}$	3000	3100	3150	3200	3300	3400	
−0.2							
−0.4					⋆		
−0.6	⋆	⋆		⋆			
−0.8			⋆	⋆			
−1.0						⋆	

$[M/H]$	+0.2	0.0	−0.2	−0.4	−0.6	−0.8	−1.0
3000							
3100							
3150						⋆	
3200	⋆			⋆	⋆	⋆	⋆
3300	⋆	⋆	⋆		⋆		
3400							⋆

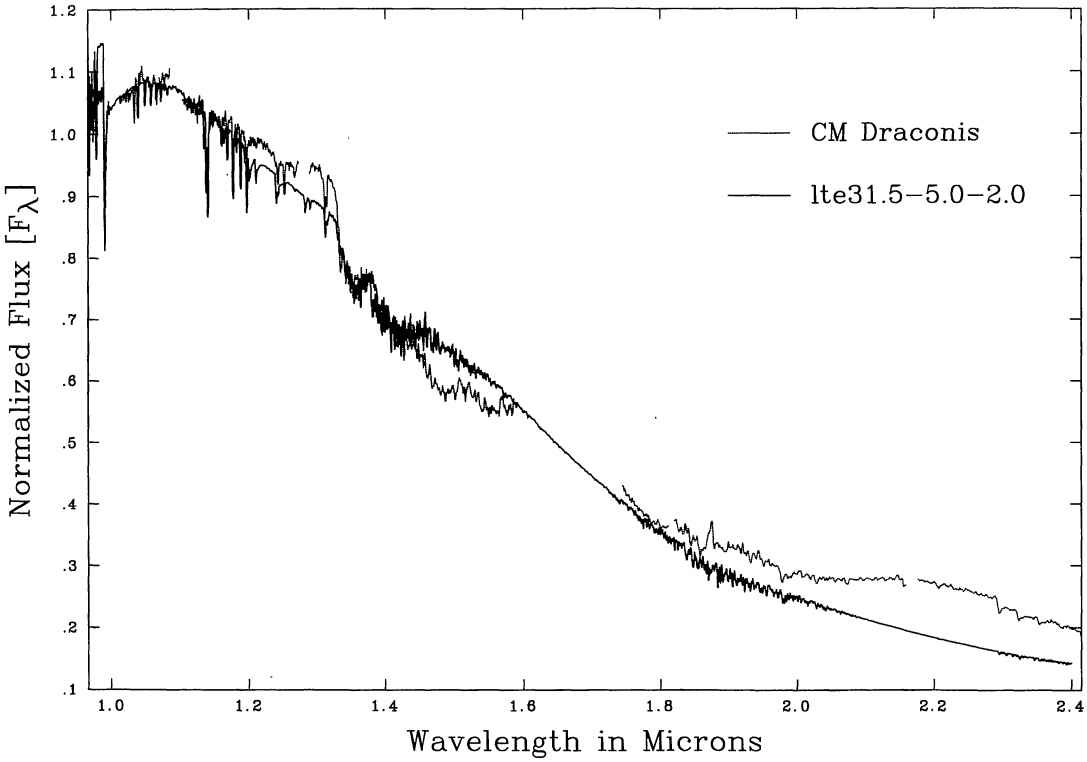

Figure 10. SED comparison of synthetic and observed spectrum. The models have been computed at $T_{\rm eff}=3150$ K with [M/H] $=-2.0$. This comparison shows how very low-metallicity models do not fit the SED.

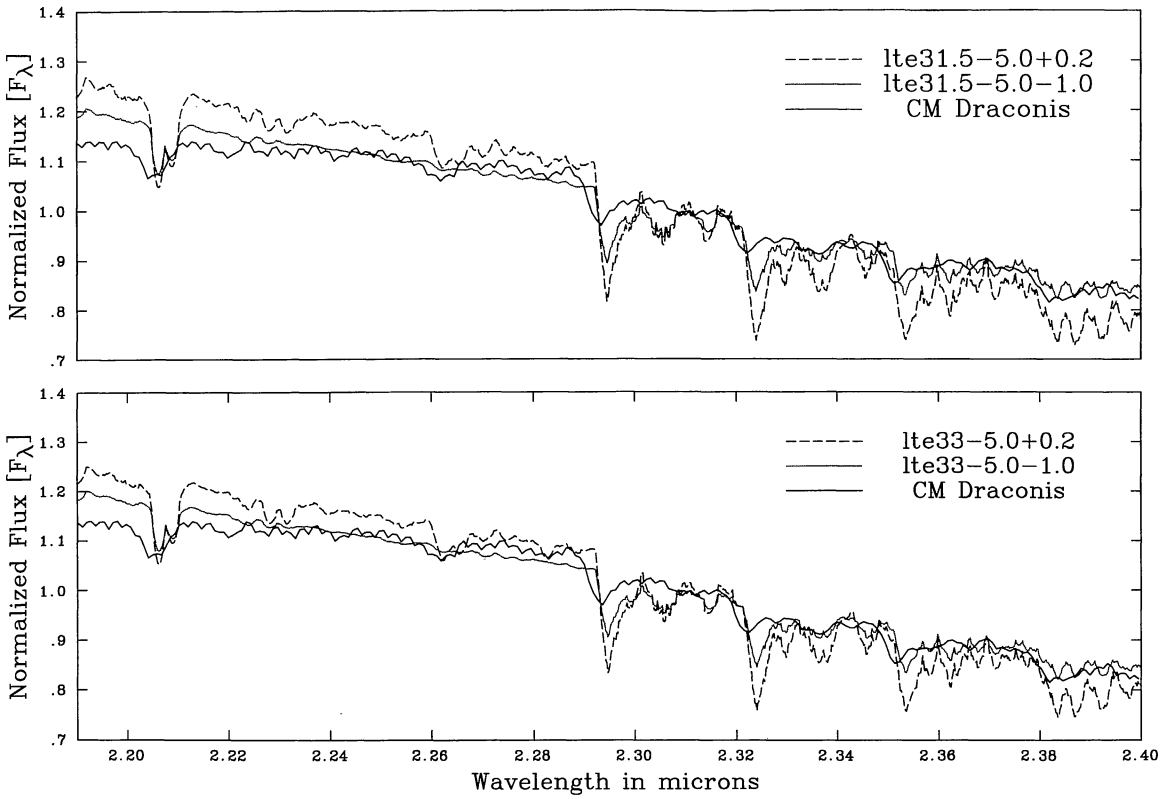

Figure 11. Detailed comparison of models with different metallicities. Top: [M/H] = +0.2, −1.0 at $T_{\rm eff}$ = 3150 K. Bottom: [M/H] = +0.2, −1.0 at $T_{\rm eff}$ = 3300 K.

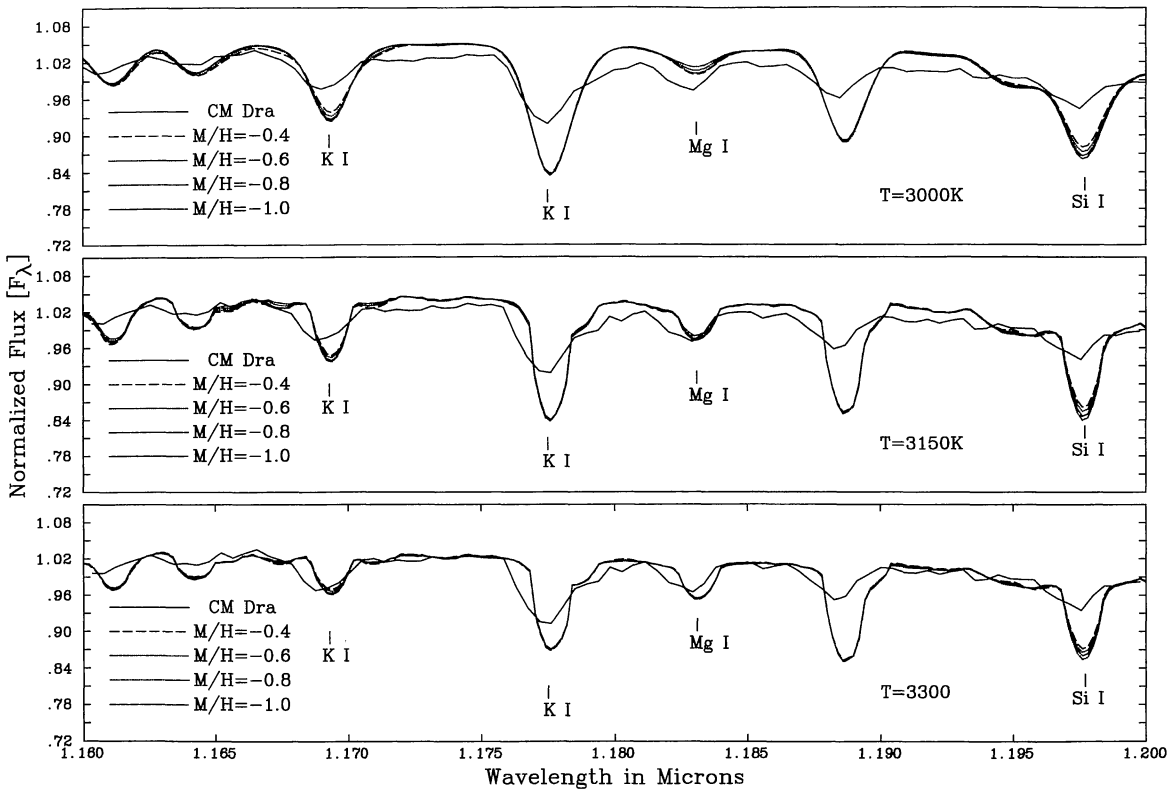

Figure 12. Small region of the observed spectrum (1.16 to 1.20 μm) compared with models at different effective temperatures. Top: $T_{\rm eff}$ = 3000 K; middle: $T_{\rm eff}$ = 3150 K; bottom: $T_{\rm eff}$ = 3300 K. For each temperature, four metallicities are compared: [M/H] = −0.4, −0.6, −0.8 and −1.0.

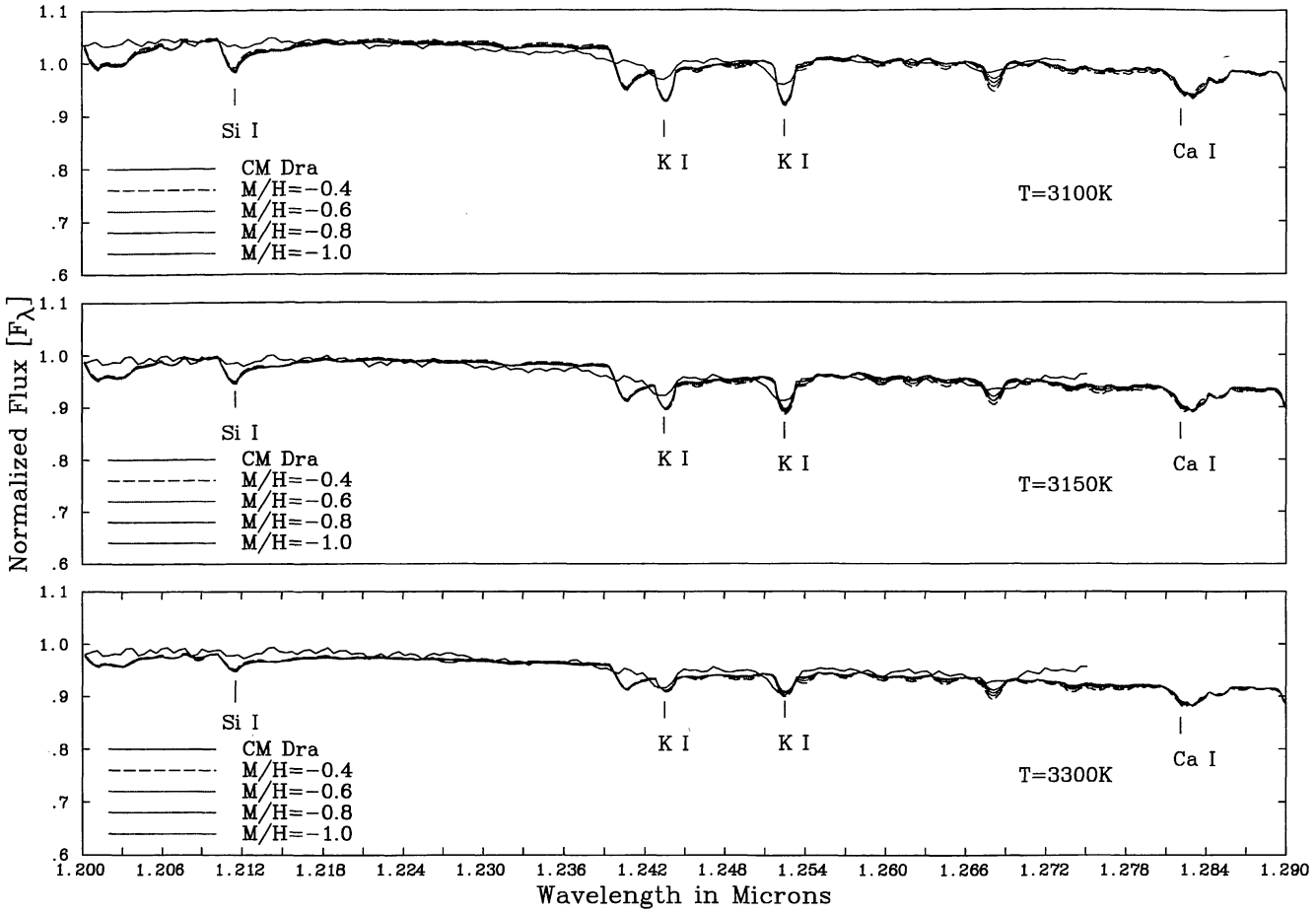

Figure 13. Comparison of a small region of the observed spectrum (1.20 to 1.29 μm) with models at different effective temperatures. Top: $T_{\rm eff}=3100$ K; middle: $T_{\rm eff}=3150$ K; bottom: $T_{\rm eff}=3300$ K. For each temperature, four metallicities are compared: [M/H] = −0.4, −0.6, −0.7 and −1.0. There are no observational data beyond 1.272 μm, when an emission line was present and has been removed.

but get nearer to the observations as the metallicity is lowered. This behaviour is shown by similar comparisons for the other two subregions.

We then compared the four subregions for all the temperatures at the metallicities of −1.0, −0.8, −0.6 and −0.4. Figs 12 and 13 show examples of such a comparison for $T_{\rm eff}=3000$, 3100, 3150, and 3300 and 3400 K.

Jones et al. (1996) show a spectral sequence from 1.16 to 1.22 μm, where strong atomic features are sensitive to different temperatures and metallicities: in particular, we notice that the strong K I line at 1.177 μm decreases in strength as the temperature increases. We find the same effect in Fig. 11, and overall we note that the observed K I line is matched better by the model at 3300 K. Some detailed examples are as follows.

(1) In the 1.16–1.20 μm region, the K I lines at ∼1.169 and 1.177 μm, and the Si lines at ∼1.198–1.199 μm are all better fitted by higher temperatures models. It is interesting to note that the K I line at 1.169 μm seems to be too strong in the 3300-K model, but too weak in the 3400-K one. The 1.177-μm K I line is better fitted by the 3400-K model.

(2) In the 1.20–1.35 μm region, the K I lines at 1.2432 and 1.2522 μm are well reproduced by the 3100-K models, while the Ca I lines at 1.3034 and 1.3086 μm are better fitted at 3200 K.

Table 6. The best model fit for each strong feature considered in the infrared region as a function of the effective temperature and of metallicity.

λ	*Element*	$T_{\rm eff}$	[*M*/*H*]
0.9961	NaI	3200	−1.0
1.1690	KI	3400	−1.0
1.1770	KI	3300	−0.8
1.1820	MgI	3300	−0.6
1.2032	Si	3300	−1.0
1.2084	MgI	3300	−1.0
1.2104	Si	3300	−1.0
1.2432	KI	3150	−1.0
1.2522	KI	3150	−1.0
2.2056	NaI	3150	−1.0
2.2084	NaI	3150	−1.0
2.2651	CaI	3300	−1.0
2.3348	NaI	3300	−1.0
2.3379	NaI	3300	−1.0

Table 6 lists the best match in effective temperature for each strong line considered. The metallicity sensitivity is relatively small; however, for completeness, the table lists the best match in metallicity as well.

So far, our analysis is based on a general flux distribution match and on the profiles of strong lines. However, strong

lines do not appear to be sensitive to metallicity changes; moreover, they are more subject to saturation and chromospheric activity effects. Furthermore, many of these lines are blended, so a different approach is explored below.

7.3 Detailed spectral analysis

Our preliminary spectral analysis reduces the metallicity range to between -0.6 and -1.0, while candidate effective temperatures range from 3150 to 3400 K. A more detailed analysis was performed by reversing the process of identification. We used the models' line identification list to find metal lines sensitive to both metallicity and temperature changes. We tried to match these lines with the observations. These weak lines should be less subject to saturation effects. A problem with this procedure is that the observed spectra are at a lower resolution than the scale of line blending. This makes the above identification harder and will introduce systematic errors in the derived parameters. For a more accurate derivation, higher resolution observations would be required.

We divided the spectral region of 1.0 to 2.4 μm into 40 subregions. For each subregion we applied the instrumental profile to the models to match the observations. Many subregions were excluded, either because the resolution was too low for identifying any features present or because of 'contamination' by water bands. The region between 1.4 and 1.6 μm is an example of a 'contaminated' subregion.

Figs 14 and 15 show some of these subregions for models with $T_{\rm eff}=3150$, 3200, and 3300 and 3400 K. Table 7 lists the best effective temperature and metallicity match for each reliable atomic line. Again, as for Table 6, the comparison has been made by eye.

(1) From 1.11 to 1.14 μm the 3300-K model at metallicity -1.0 gives a generally better fit, in particular to the Na I at 1.1385 μm.

(2) From 1.14 to 1.18 μm the $T_{\rm eff}=3200$ and 3300-K models give the best fit, although it is difficult to fix the metallicity. For example, the K I line at 1.169 μm is matched better by the -1.0 model if $T_{\rm eff}=3300$ K is chosen, while a metallicity of -0.6 gives a better fit to the observations at $T_{\rm eff}=3200$ K.

(3) At 1.253 μm, the K I line is better matched by the 3200-K, [M/H] $=-1.0$ model. However, we note that at 3300 K the line is too weak and a metallicity of -0.6 gives a better fit, while at 3200 K it is too strong and at [M/H] $=-1.0$ it generally gives a better fit. Indeed, this is confirmed by the model at $T_{\rm eff}=3400$ K, where the K I line is far too weak at both metallicities.

In Table 8, we give the best metallicity match within each effective temperature. This final analysis suggests that the high-temperature and low-metallicity models give a better match to the observed infrared spectrum of CM Dra; in particular, [M/H] seems to lie between -1.0 and -0.4. This conclusion is consistent with the results of a comparison of CM Dra to a sample of spectra stars with similar temperatures and different metallicities such as Gl 213 ($T_{\rm eff}=3150$ K, [M/H] $=0.0$), Gl 206 ($T_{\rm eff}=3300$ K, [M/H] $=+0.1$) (Leggett et al. 1996), Gl 699 ($T_{\rm eff}=3100$ K,

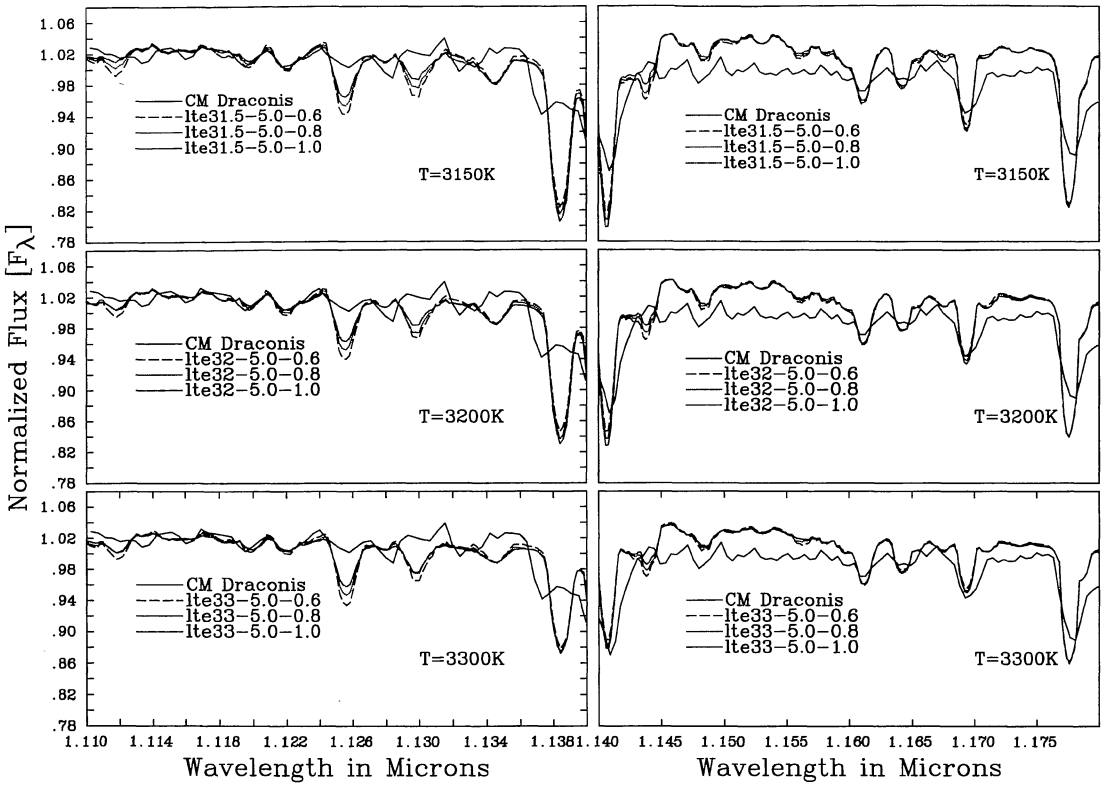

Figure 14. Comparison of synthetic models for two neighbouring regions. Left top, middle, bottom: comparisons of the region 1.11 to 1.13 μm at respectively $T_{\rm eff}=3150$, 3200 and 3300 K for the metallicities of -0.6, -0.8 and -0.10. Right top, middle, bottom: same comparison for the region 1.14 to 1.18 μm.

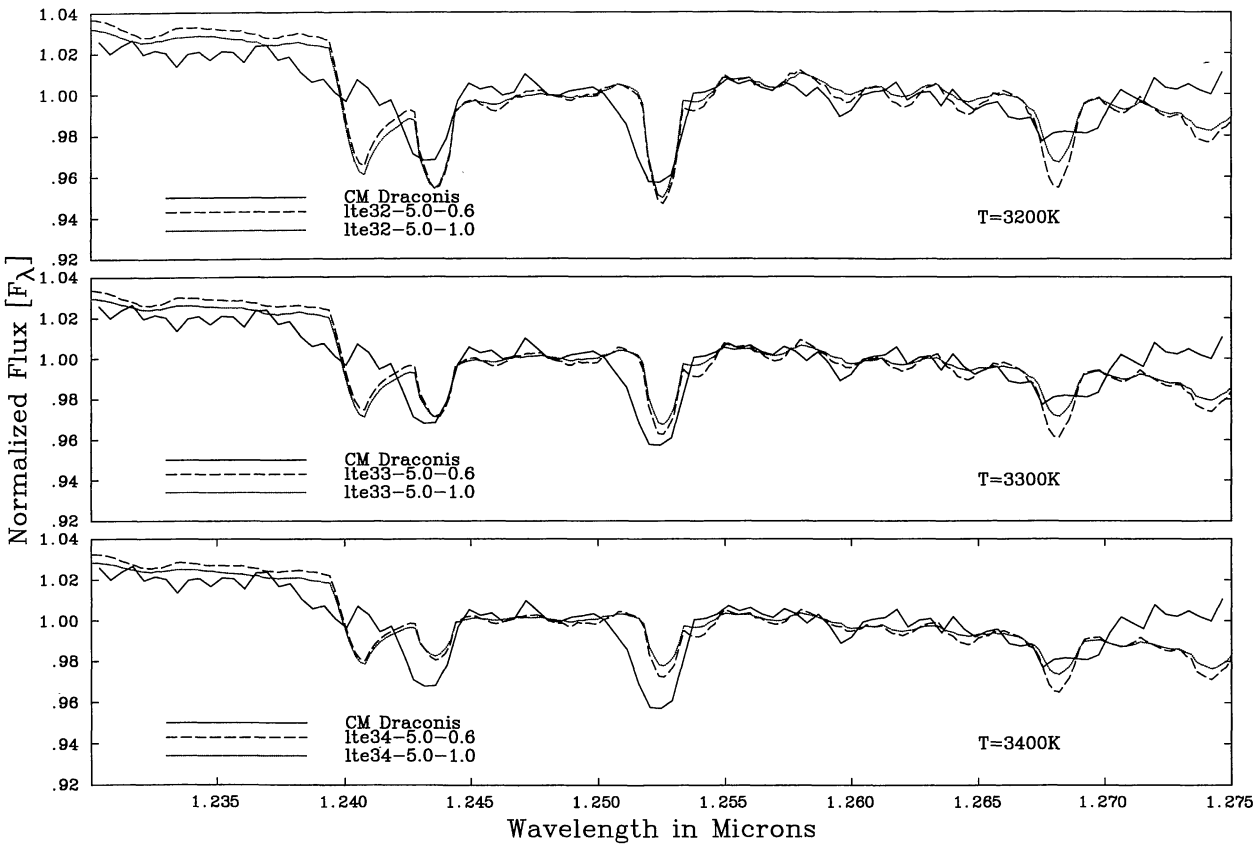

Figure 15. Comparisons between observed spectra and models (1.20 and 1.25 μm). Top: $T_{\rm eff}=3200$ K, [M/H] $=-0.6$ and -1.0; middle: $T_{\rm eff}=3300$ K, [M/H] $=-0.6$ and -1.0; bottom: $T_{\rm eff}=3400$ K, [M/H] $=-0.6$ and -1.0.

Table 7. The best model fit for each atomic line considered as a function of the effective temperature and metallicity for the infrared region.

$\lambda(\mu m)$	*Element*	$T_{\rm eff}$	$[M/H]$
1.11179	AlI		−1.0
1.111973	FeI	3200	−0.8/ − 1.0
1.11631	CrI		−1.0
1.11963	NiI	3300	−0.8
1.11984	NiI	3300	
	NiI	3200	−0.6
1.12214	AlI	3150	−0.8/ − 1.0
1.12559	FeI		−1.0
1.12974	FeI		−1.0
1.13819	NaI	3150	−0.6
1.13846	NaI	3300	
1.18303	MgI	3300	−1.0
1.19156	FeI	3300	−1.0
1.18307	MgI	3300	−1.0
1.19541	TiI	3300	−1.0
1.20198	SiI	3400	−0.8
1.21192	MgI	3400	−1.0
1.24034	KI	3300	−0.6
1.24360	KI	3300	
1.25264	KI	3300	−0.6
	KI	3200	−1.0
1.25706	TiI	3200	−0.8
1.25998	TiI	3400	−1.0
1.26800	NaI	3400	−1.0
2.20865	NaI	3300	−1.0
2.20899	NaI	3300	−0.6
	NaI	3200	−0.8

Table 8. Best metallicity match within each effective temperature after a detailed spectral analysis of this infrared observed region.

$T_{\rm eff}$	3000	3100	3150	3200	3300	3400
0.0						
−0.2						
−0.4	⋆	⋆				
−0.6						
−0.8						
−1.0			⋆	⋆	⋆	⋆

[M/H] $=-0.5$) (Jones et al. 1996; Leggett et al. 1996) and Gl 299 ($T_{\rm eff}=3050$ K, [M/H] $=-0.5$) (Jones et al. 1996; Leggett et al. 1996). However, we note that the effective temperature scale of the sample of stars from Leggett et al. (1996) was based on the earlier 'Base' model grid (Allard & Hauschildt 1995) which is substantially different from the present improved models (see Allard et al. 1997).

8 HELIUM ABUNDANCE

Because of the high accuracy to which masses and radii are known, it has been pointed out that CM Dra could be a test system to determine primordial helium abundances (Paczyński & Sienkiewicz 1984). Metcalfe et al. (1996) followed the method employed by Paczyński & Sienkiewicz for obtaining helium abundances by comparing the nuclear luminosity with the observed one. They obtained the rather high values of $Y_{\rm A}=0.32\pm0.04$ and $Y_{\rm B}=0.31\pm0.04$ com-

pared to quoted primordial helium abundances such as Olive & Steigman's (1995) values of $Y_p = 0.232 \pm 0.003$. This may be due to the neglect of systematic errors such as non-LTE effects in computations of the helium abundance for hot stars (Sesselov & Goldwirth 1995), although it may also arise from a lack of consideration of metallicity. Fig. 2 in Burrows et al. (1993) shows the effect of varying the helium abundance between 0.22 and 0.28 for solar metallicity models, and between 0.22 and 0.25 for zero-metallicity models. For masses between 0.1 and 0.2 $M_\odot$, it can be seen that the luminosities of the models are much more sensitive to metallcity than to helium abundance. According to this, a much more reliable determination of the metallicity of CM Dra ($M/M_\odot \sim 0.2$) could help to resolve the discrepancy in the value for its helium abundance.

9 RESULTS AND CONCLUSIONS

Fig. 16 summarizes Tables 3, 4, 5 and 7. It also puts our findings for the range of effective temperature. Based on a direct comparison of synthetic and observed spectra in the near-infrared and optical regions, we have investigated the effective temperature and metallicity of the binary system CM Dra. During the course of our analysis, we found some inconsistencies that were to be expected.

(1) The comparison of the general flux distribution for both the optical and infrared regions implied that a metallicity of -1.0 is too low for the system.

(2) An analysis of the infrared spectra suggested low metallicities (as low as -1.0) and/or higher temperatures (as high as 3300 K) for an optimal fit.

(3) A detailed analysis of the optical spectrum leads to systematically lower effective temperatures (~ 3200 K) and higher metallicity (~ -0.6) than a similar analysis of the infrared spectra.

Some of the inconsistencies noted can be explained by the systematic calibration errors between the optical and infrared observations as well as (i) the known incompleteness of the water and TiO line lists used in the models, and (ii) the lack of an FeH line list. Also, CM Dra is close to the regime where grain formation may begin to affect the photosphere and spectral distribution of late-M dwarfs. Some condensation may cause elemental abundances of line-forming elements such as Fe I, Ti I, K I, Ca I and Na I to drop by factors of 2–10 and simulate the aspect of a hotter star in high-redsolution analysis of line strengths. Models incorporating the effects of some grain formation have been computed by Tsuji, Ohnaka & Aoki (1996a) and Tsuji et al. (1996b), who argued that grain formation is the event responsible for this long-standing infrared discrepancy. However, their models only begin to show strong grain formation for $T_{\rm eff} \leq 2700$ K, i.e., spectral types later than about M6 (Jones & Tsuji 1997), leaving hotter stars unaffected and their infrared discrepancies unexplained.

We are, however, led to conclude that, although the systematic differences of the optical and infrared derived parameters arise partly from both the observational uncertainties and the incompleteness of the current line lists, it is

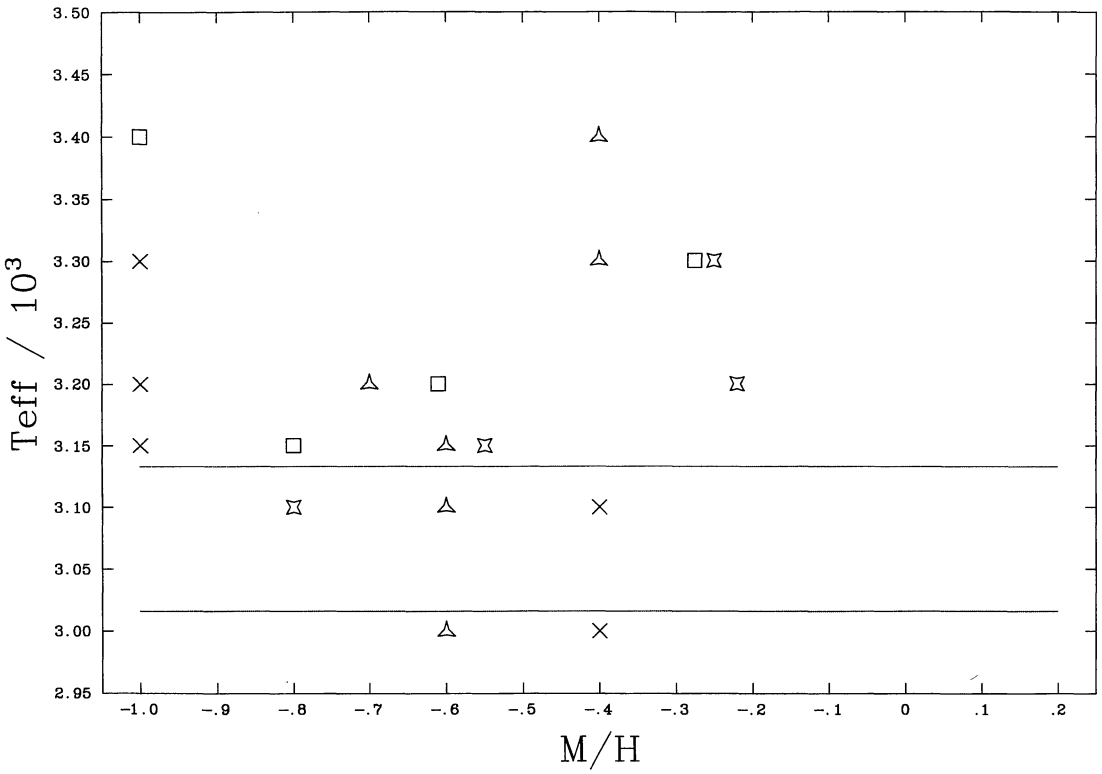

Figure 16. Summary of results. Square = infrared results after a SED analysis (Table 5); Star (four vertices) = optical results after a SED analysis (Table 3); Cross = infrared results after a detailed analysis (Table 7); Star (three vertices) = optical results after a detailed analysis (Table 4). The dotted lines show the range of Stefan–Boltzmann temperatures obtained from the flux section (Section 4).

unlikely that any single metallicity parameter will reproduce all the spectral features. This suggests that CM Dra could be chemically peculiar and might not be reproduced by models based on solar abundances.

Better spectral coverage and resolution of the observations are necessary for a confirmation of CM Dra chemical peculiarity and a more accurate determination of the effective temperature, metallicity and abundance parameters of CM Dra.

ACKNOWLEDGMENTS

We thank the staff at the United Kingdom Infrared Telescope and at the Steward Observatory for assistance with the observations. This work was partly supported by the UK Particle Physics and Astronomy Research Council. SV thanks Drs P. B. Byrne and M. Zboril for useful comments, and Dr A. E. Lynas-Gray for carefully proof-reading this manuscript. PHH gratefully acknowledges support from NASA ATP grant NAGW 5-30128 and NASA LTSA grant NAGW 5-3019. Some of the calculations presented in this paper were performed on the Cray C90 of the SDSC and on the IBM SP2 of the CTC under a generous allocation of computer time under the MetaCenter program to PHH.

REFERENCES

Allard F., Hauschildt P. H., 1995, ApJ, 445, 433
Allard F., Hauschildt P. H., Miller S., Tennyson J., 1994, ApJ, 426, L39
Allard F., Hauschildt P. H., Alexander D. R., Starrfield S., 1997, ARA&A, 35, 137
Baraffe I., Chabrier G., Allard F., Hauschildt P. H., 1997, ApJ, in press
Burrows A., Hubbard W. B., Saumon D., Lunine J. I., 1993, ApJ, 406, 158
Chabrier G., Baraffe I., 1995, ApJ, 451, 29 (CB95)
Colina L., Bohlin R. C., 1994, ApJS, 108, 1931
Collins J. G., Faij T. D. J., 1974, J. Quant. Spectrosc. Radiat. Transfer, 14, 1259
Gizis J., 1997, AJ, 113, 806
Jones H. R. A., Tsuji T., 1997, ApJ, 480, L89
Jones H. R. A., Longmore A. J., Allard F., Hauschildt P. H., Miller S., Tennyson J., 1995, MNRAS, 277, 767
Jones H. R. A., Longmore A. J., Allard F., Hauschildt P. H., 1996, MNRAS, 280, 77
Jørgensen U. G., 1994, A&A, 284, 179
Horne K., 1986, PASP, 98, 609
Lacy C. H., 1977, ApJ, 218, 444
Leggett S. K., 1992, ApJS, 82, 351
Leggett S. K., Allard F., Berriman G., Dahn C. C., Hauschildt P. H., 1996, ApJS, 104, 177
Metcalfe T. S., Mathieu R. D., Latham D. W., Torres G., 1996, ApJ, 456, 356
Miller S., Tennyson J., Jones H. R. A., Longmore A. J., 1994, in Jørgensen U. G., ed., Lecture Notes in Physics Vol. 428, Molecules in the Stellar Environment. Springer, Berlin, p. 296
Monet D. G., Dahn C. C., Vrba F. J., Harris H. C., Pier J. R., Luginbuhl C. B., Ables H. D., 1992, AJ, 103, 638
Oke J. B., 1990, AJ, 99, 1621
Olive K. A., Steigman G., 1995, ApJS, 97, 49
Paczyński B., Sienkiewicz R., 1984, ApJ, 286, 332
Puxley P. J., Ramsay S. K., Beard S. M., 1992, in Grøsbol P., ed., Proc. 4th ESO/ST-ECF Data Analysis Workshop
Ruciński S. M., 1978, Acta Astron., 28, 167
Sasselov D., Goldwirth D. S., 1995, ApJ, 444, L5
Schryber J. H., Miller S., Tennyson J., 1995, J. Quant. Spectrosc. Radiat. Transfer, 53, 373
Steele I. A., Jameson R. F., Hambly N. C., 1993, MNRAS, 263, 647
Tsuji T., Ohnaka K., Aoki W., 1996, A&A, 305, 1
Tsuji T., Ohnaka K., Aoki W., Nakajima T., 1996, A&A, 308, 29
van Altena W. F., Lee J., T.-L., Hoffleit D., 1995, Catalogue of Trigonometric Parallaxes. Yale Univ. Observatory